Nanoscale

Accepted Manuscript

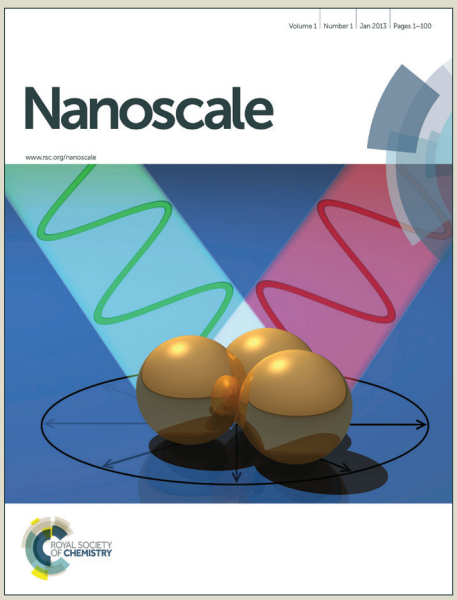

ROYAL SOCIETY OF CHEMISTRY

www.rsc.org/nanoscale

Cite this: Nanoscale, 2012, XXXX

www.rsc.org/ees

paper

Hierarchical MoS_2 nanosheets/active carbon fiber cloth as binder-free and free-standing anodes for lithium-ion batteries

Chao Wang,[a,b†] Wang Wan,[a†] Yunhui Huang,[b]* Jitao Chen,[a]* HengHui Zhou,[a]* XinXiang Zhang,[a]

Received (in XXX, XXX) Xth XXXXXXXXX 20XX, Accepted Xth XXXXXXXXX 20XX

DOI: 10.1039/b000000x

Owing to the layered structure and high theoretical capacity, MoS_2 has attracted more and more interest as a potential anode material for lithium-ion battery. However, it suffers from rapid capacity decay and low rate capability. In this work, we introduce a novel hierarchical material consisting of ultrathin MoS_2 nanosheets grown on the surface of an active carbon fiber (ACF) cloth fabricated by a facile morphogenetic process. The ACF cloth acts as both a template and a stabilizer. The obtained MoS_2/ACF cloth composite possesses hierarchical porosity and an interconnected framework. Serving as a free-standing and binder-free anode, it shows high specific capacity and excellent reversibility. A discharge capacity as high as 971 mAh g^{-1} is attained at a current density of 0.1 A g^{-1}, and the capacity fade is only 0.15% per cycle within 90 cycles. Even after 200 cycles at a high current density of 0.5 A g^{-1}, the composite still shows a capacity of 418 mAh g^{-1}. The superior electrochemical performance of MoS_2/ACF can be attributed to its robust structure and to the synergistic effects of ultrathin MoS_2 nanosheets and ACF. This single-component anode that we propose benefits from a simplified electrode preparation process. The morphogenetic strategy used for the material production is facile but effective, and can be extended to prepare other metal sulfides with elaborate textural characteristics.

Introduction

Lithium-ion batteries (LIBs) have been widely used in portable electronic devices in the last two decades and recently have attracted extensive attention as power sources for electric or hybrid electric vehicles.[1-3] To cater to the requirements of application in vehicles, exploring new electrode materials with high capacity and excellent stability is crucial for high-performance LIBs. Recently, layered transition metal sulfides (MS_2, M = Ti, W, Mo, In, etc.) have gained widespread interest because of their unique physical and chemical properties.[4-7] In these materials, the layered structure is formed through van der Waals interaction between the nanosheets, giving rise to wide interlayer spaces that allow the introduction of small ions. The small Li ions with a low charge can be readily intercalated into and extracted from the interlayer spaces.[8-10] Hence, the layered transition metal sulfides are potential anode materials and have been investigated extensively for next-generation LIBs.[11]

MoS_2 is a stable layered sulfide, which undergoes a four-electron transfer reaction during the charge-discharge process, leading to a high theoretical capacity.[11-13] However, the poor cycling stability and low rate capability of MoS_2 are the main barriers to limit its practical application.[12] To overcome these barriers, many researchers have devoted to enhancing the electrochemical performance of MoS_2 by constructing uniform hybrid structures of MoS_2 with carbon, carbon nanotubes, graphene, etc. For example, Zhang et al. fabricated MoS_2/carbon composites with one-dimensional nanostructures (nanorods and nanotubes) by precisely controlling H_2S gas sulfidation of MoO_x/polyaniline hybrid, and showed that the composite with nanotubes exhibited superior performance than that with nanorods.[14] Ding et al. employed a simple glucose-assisted hydrothermal method to directly grow MoS_2 nanosheets on carbon nanotube (CNT) backbone to achieve CNT@MoS_2 composite, and obtained significantly enhanced lithium storage properties compared with pure MoS_2 nanoflakes.[15] Wang et al. fabricated a MoS_2-composite thin film with single-walled carbon nanotube (SWNT) via a filtration/wet transfer technique, which showed an improved electrochemical performance for Li-ion storage.[16] Chang et al. synthesized layered MoS_2/graphene composites with different Mo/C ratios by a facile L-cysteine-assisted solution phase method, and found that the composite with a Mo/C molar ratio of 1:2 showed the best performance.[17] Yu et al. prepared graphene/MoS_2 nanoflake arrays with three-dimensional (3D) architecture; such 3D architecture exhibited remarkably high rate performance due to stable structure and large electrode-electrolyte interfacial area.[18] In general, most of the MoS_2/carbon composites employ either graphene or carbon nanotubes as the carbon substrates, which need to use the traditional way to further prepare the electrodes with conductive carbon and binder. This may encounter some problems, such as exfoliation of active materials from the current collector, loss of entire composite capacity, etc. If the active material can be directly coated onto some special substrate, a free-standing and binder-free electrode can be attained to overcome the disadvantage issues and achieve high performance.[19-21] Recently, Yu et al. fabricated a 3D hierarchical MoS_2 nanoflake arrays/carbon cloth

via a hydrothermal process, and obtained good rate discharging/charging stability when used as anodes for flexible LIBs.[22]

In this work, we developed a simple dissolution and sintering method to fabricate a flexible composite material by directly growing ultrathin MoS_2 nanosheets on the surface of active carbon fiber (ACF) cloth to attain the hierarchical MoS_2/ACF cloth composite, as illustrated in Fig. 1. The ACF cloth acts as both template and conductivity framework. The interconnected carbon fibers provide fast transport paths for electrons and lithium ions. Most importantly, the MoS_2/ACF cloth can be used directly as a free-standing and binder-free electrode. In such a hierarchical structure, the ultrathin MoS_2 nanosheets can greatly reduce the solid-state diffusion length for both lithium ions and electrons because of the confinement effect. Furthermore, the MoS_2 nanosheets, which are uniformly grown on the ACF cloth to form a porous surface structure, can provide a large electrode-electrolyte interfacial area, leading to an improved rate performance. On the other hand, the flexible MoS_2/ACF cloth can buffer the large volume change caused in MoS_2 during cycling. The hierarchical structure keeps stable for Li-ion insertion and extraction, and is hence expected to exhibit a good charge-discharge performance during cycling. Being evaluated as an anode material for LIBs, the as-formed ultrathin MoS_2 nanosheets on ACF cloth with a hierarchically porous configuration exhibited high reversible lithium storage capacity, long cyclability and excellent rate capability.

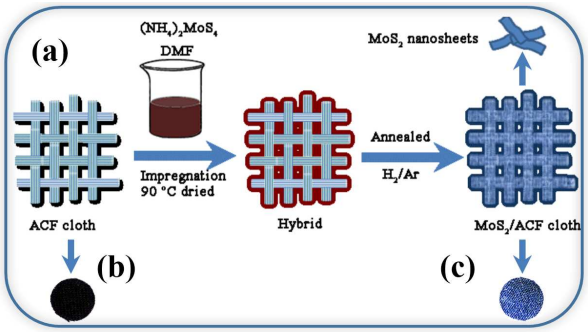

Fig. 1 (a) Schematic illustration of the synthesis process and structure of the as-designed MoS_2/ACF cloth. Photographs of the free standing ACF cloth punched discs taken (b) before and (c) after loading MoS_2. The color changes after loading MoS_2.

Experimental methods

Synthesis of materials

Ammonium tetrathiomolybdate $(NH_4)_2MoS_4$ was bought from J&K Chemical, with a purity of 99%. MoS_2 powders (AR) and sublimed sulfur (CP) were obtained from Sinopharm Chemical Reagent. ACF cloth was obtained from Anhui Jia Li Qi Aerospace Carbon fiber Co, Ltd. The AFC cloth was used after sonication in ethanol and heating at 800 °C for 2 h in a 5% H_2/Ar atmosphere. The AFC cloth acted as a substrate for loading MoS_2 nanosheets. Fig. 1 schematically illustrates the two-step process used for the synthesis of the MoS_2/ACF cloth. In a typical procedure, $(NH_4)_2MoS_4$ (0.25 g) was added to 20 mL dimethylformamide (DMF) to obtain a 1.25 wt% solution. The solution was sonicated for 20 min before use. The ACF cloth was immersed into the solution for 15 min, taken out, and dried at 90 °C for 30 min in a vacuum oven. The immersion and drying processes were repeated for five times. Thereafter, the as-formed product was annealed at 750 °C for 2 h (ramp rate = 10 °C min^{-1}) in 5% H_2/Ar atmosphere. The conversion from $(NH_4)_2MoS_4$ to MoS_2 in the presence of H_2 gas can be described by the following equation.[23]

$$(NH_4)_2MoS_4 + H_2 \rightarrow 2NH_3 \uparrow + 2H_2S \uparrow + MoS_2$$

It is worth noting that elemental sulfur was added during the annealing process to avoid the reduction of MoS_2.[23] After annealing, the color of the carbon paper changed from black to blue,[24] as shown in Fig. 1. The obtained MoS_2/ACF cloth paper was used for further characterization and employed directly as an electrode.

Characterization

The phases of the composites were characterized by X-ray diffraction (XRD) on a Rigaku D/MAX-2000 diffractometer (Japan) using Cu Kα radiation (wavelength = 0.15406 nm). The morphology and microstructure were observed by field-emission SEM (S4800, Hitachi) and TEM (Tecnai F20). The elemental composition and mapping were conducted via local chemical analysis performed by SEM-EDX with an EDAX APLLO XP detector on SEM. Raman spectroscopy was performed with a LabRam ARAMIS confocal micro Raman spectrometer (Horiba Jobin Yvon) with an excitation wavelength of 633 nm. XPS measurement was carried out on an Axis Ultra (Kratos Analytical Ltd.) imaging photoelectron spectrometer using a monochromatized Al Kα anode. The energy calibrations were made against the C 1s peak to eliminate the charging of the sample during analysis.

Electrochemical measurements

The electrochemical properties of the composite were evaluated by using coin cells with lithium metal as the counter electrode and Celgard 2400 membrane as the separator. The flexible MoS_2/ACF cloth was punched into circular disks with a diameter of 12 mm to be directly used as the working electrode without further treatment. The CR2032 coin cells were assembled in an argon-filled glove box (Master 100 Lab, Braun, Germany) where moisture and oxygen concentrations were strictly controlled to below 1 ppm. Pressure was applied to the ACF cloth when the coin cells were fabricated. The reference MoS_2 powder was fabricated into an electrode using the traditional method as described in ESI. The commercial electrolyte containing 1 mol L^{-1} $LiPF_6$ in a mixture of ethylene carbonate (EC) and dimethyl carbonate (DMC) (v/v=1:1) was used. The cells were galvanostatically charged and discharged between 0.005 and 3 V versus Li^+/Li on a Land CT2001A battery tester. CV was carried out on a CHI660D electrochemical workstation (CH Instruments, China) at a scan rate of 0.1 mV s^{-1} at voltages ranging from 0 to 3 V versus Li^+/Li. EIS was measured on the coin cell by an electrochemical workstation (Autolab PG302N, Netherlands) with an applied sinusoidal excitation voltage of 5 mV in the frequency range 100 kHz–0.1 Hz.

Results and discussion

Fig. 1a schematically illustrates the synthesis process used for the in situ growth of MoS_2 nanosheets on the surface of ACF cloth. The surface changes from smooth to porous because of the anisotropic growth of the ultrathin MoS_2 nanosheets. The porous

nature of the cloth is favorable for electrochemical reaction of lithium ions. The formation of MoS_2 nanosheets is mainly due to its layered structure held by van der Waals interaction.[24] The dark blue color, which totally replaces the black color of ACF cloth, is consistent with the color of the reported MoS_2 freestanding paper,[24] which indicates the presence of uniformly grown MoS_2 nanosheets on the surface of the ACF cloth (see Fig. 1b-c).

Fig. 2a shows the X-ray diffraction (XRD) patterns of ACF cloth and hierarchical MoS_2/ACF. The pattern of the MoS_2/ACF can be indexed as the orthorhombic phase of MoS_2 (JCPDS No. 37-1492). The MoS_2/ACF shows four major diffraction peaks at 2θ = 14.2, 32.8, 39.7 and 58.3°, which can be assigned to the (002), (100), (103) and (110) planes of hexagonal MoS_2 phase, respectively.[25] The (002) diffraction corresponding to a *d*-spacing of 0.62 nm agrees well with that observed in the TEM image, indicating that the layered MoS_2 grows well along the *c* axis during annealing. The board peak centered at 2θ = 23° is a typical diffraction of amorphous carbon caused by the ACF cloth.

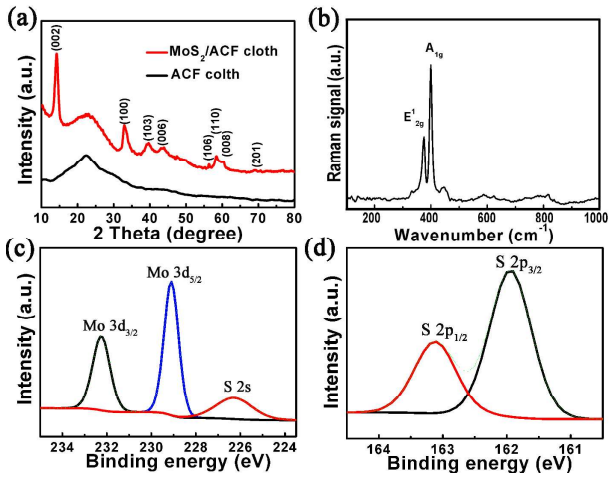

Fig. 2 (a) XRD patterns of the ACF cloth and the MoS_2/ACF cloth. (b) Raman spectrum of the MoS_2/ACF cloth. XPS profiles corresponding to the binding energies of (c) Mo 3d (d) S 2p acquired from the MoS_2/ACF cloth.

Fig. 2a The Raman spectra acquired from the hierarchical MoS_2/ACF cloth is displayed in Fig. 2b. After annealing, two characteristic peaks are observed at 381.5 and 405.4 cm^{-1}, which correspond to the E^1_{2g} and A_{1g} modes of the hexagonal MoS_2, respectively. These Raman shifts come from the first order Raman vibration modes within the S-Mo-S layer. It has been reported that Raman spectroscopy can be used to identify the number of layers in few-layer MoS_2 crystals based on the energy difference (Δ) between the two Raman peaks.[23, 26, 27] The Δ value of the hierarchical MoS_2/ACF cloth is 23.9 cm^{-1}, indicating that in our case the MoS_2 is in an ultrathin state containing several layers.

In order to analyze the surface chemical and oxidation states of the ACF cloth after annealing with $(NH_4)_2MoS_4$ at 750 °C, X-ray photoelectron spectroscopy (XPS) was carried out. The cloth was examined directly in one piece. The survey spectra of ACF cloth and MoS_2/ACF are shown in Figs. S1 and S2. The peaks related to Mo, S, O, C and N are marked out in the spectra. The peak of carbon looks very strong in the spectrum of ACF cloth (Fig. S1), but it becomes very weak as compared with Mo and S in the spectrum of MoS_2/ACF (Fig. S2), indicating that the surface of ACF cloth is almost covered by MoS_2. Figs. 2c and 2d show the XPS profiles of Mo 3d and S 2p acquired from the MoS_2/ACF cloth. The high resolution Mo 3d peak (Fig. 2c) shows two sub-peaks at the binding energies of 229.3 and 232.5 eV, which can be attributed to the doublet Mo $3d_{3/2}$ and Mo $3d_{5/2}$, respectively, of Mo^{4+} in MoS_2. A small S 2s peak is centered at 226.3 eV. In Fig. 2d, the peaks at 163.3 and 162 eV correspond to the S $2p_{1/2}$ and $2p_{3/2}$, respectively, of divalent sulfide ions (S^{2-}). All the binding energy values are consistent well with those reported for MoS_2 crystals.[23, 28-30] The results confirm that the MoS_2/ACF cloth is free of other impurities and the Mo and S exist as MoS_2 on the surface of ACF cloth.

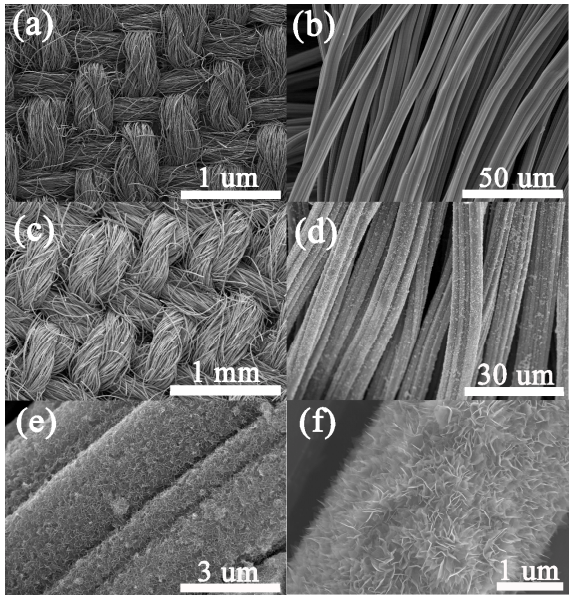

Fig. 3 (a, b) SEM images of the original ACF cloth. (c–f) SEM images of the as-obtained hierarchical MoS_2/ACF cloth.

The scanning electron microscopy (SEM) images in Fig. 3 show the morphology of the ACF cloth and the MoS_2/ACF cloth. The ACF cloth used in this work is obtained through a simple weaving method. From the images, we can see that the cloth shows a microstructure of compact bundle fibers, which is actually an artificial pseudo-two-dimensional network (Fig. 3a, b). The fasciculus with a diameter of around 20 μm is comprised of a bundle of fibers with an average diameter of around 5 μm. After impregnation of the $(NH_4)_2MoS_4$ solution and subsequent calcination in H_2/Ar atmosphere, the obtained MoS_2/ACF product exhibits perfect replication of the configuration from the original ACF cloth network (Fig. 3c, d). It is clear from Fig. 3d that the growth occurs on the surface of ACF.

Energy dispersive X-ray spectroscopy (EDX) elemental mapping was used to explore the distribution of MoS_2 in the MoS_2/ACF cloth (Fig. 4). It can be seen that Mo, S and C are uniformly distributed in the MoS_2/ACF cloth, indicating homogeneous combination of MoS_2 and ACF cloth. Interestingly, close observation confirms the presence of a large number of nanosheets uniformly grown on the surface of the ACF cloth. The thickness of the ultrathin nanosheets is about several nanometers (Fig. S4). The nanosheets are interconnected with each other, resulting in a network of MoS_2 and pores on the ACF surface. This

as-obtained MoS_2/ACF cloth combines features of both 1D and 2D structures. The ACF cloth provides a good interconnected path for electron transport to compensate for the poor electrical conductivity of MoS_2. Fig. S3 schematically shows the electron and ion transport pathways in the MoS_2/ACF cloth.

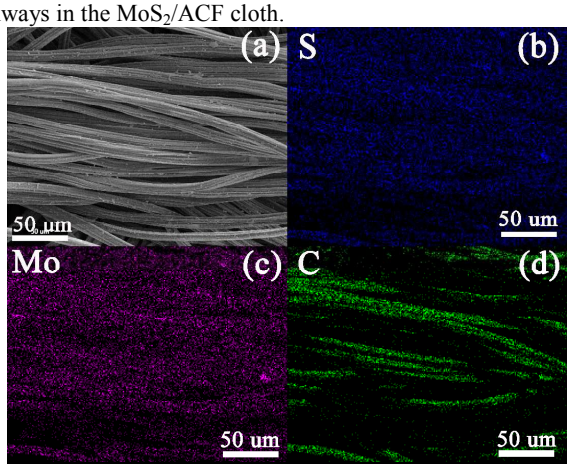

Fig. 4 (a) SEM image and corresponding EDX maps showing the distribution of (b) S, (c) Mo, and (d) C in the MoS_2/ACF cloth.

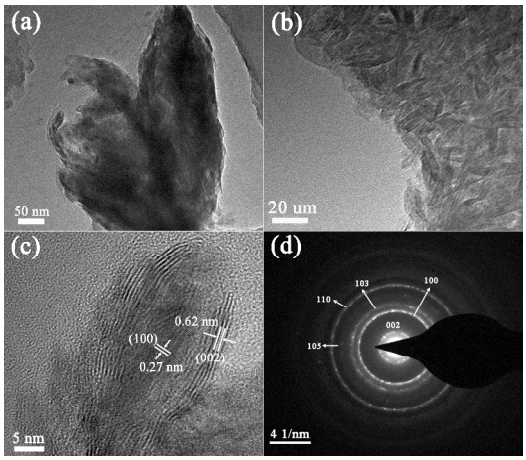

Fig. 5 Microstructure of the MoS_2/ACF cloth: (a, b) TEM image, (c) HRTEM image, and (d) selected-area electron diffraction pattern.

Transmission electron microscopy (TEM) was further used to examine the microstructure and crystallinity of MoS_2 nanosheets. The hierarchically structured MoS_2/ACF is not very clear in the TEM images since the MoS_2/ACF cloth was ground into powder and ultrasonically dispersed in ethanol during the TEM sample preparation, which caused the separation of MoS_2 nanosheets from the carbon fibers. Fig. 5 displays the flower-shaped MoS_2 flakes with the petals of the flowers growing in the same direction, which should be perpendicular to the ACF surface. The petals are the MoS_2 nanosheets that are also observed in the SEM images. The sheets grow up from the surface of carbon fibers and some of them form flower-like shapes. It can be seen from Fig. 5b that the petals of the flowers consist of many nanosized crystals that are interconnected together. From Fig. 5c, it can be seen that the thickness of the MoS_2 nanosheets is about 5 nm, which is consistent with the SEM observation. The high resolution images in Fig. 5c indicate that the well-defined layered structures of MoS_2 show an interlayer distance of 0.62 nm that can be attributed to the (002) planes, and an interlayer distance of 0.27 nm that can be indexed to the (100) planes of MoS_2. The selected area electron diffraction (SEAD) pattern in Fig. 5d can be indexed to the pure hexagonal MoS_2 phase. Five diffraction rings can be observed in the SEAD pattern, which can be indexed as the (002), (100), (103), (105) and (110) planes. The rings are cause by the presence of nanosized crystals.

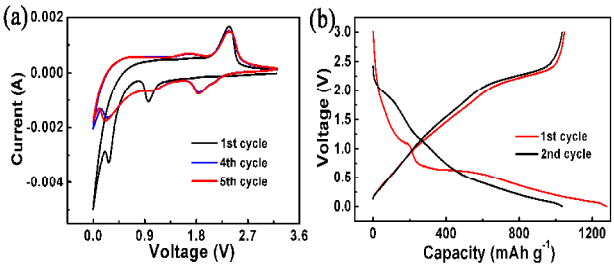

Fig. 6 (a) CVs of the MoS_2/ACF cloth electrode at 0–3 V vs. Li^+/Li recorded at a potential scanning rate of 0.2 mV s^{-1}. (b) Typical charge and discharge curves during the first and second cycles of the MoS_2/ACF cloth electrode at a current density of 200 mA g^{-1}.

The hierarchical MoS_2/ACF cloth shows an interesting architecture, which combines the advantages of both 1D and 2D structures. The interconnecting carbon fibers and MoS_2 nanosheets are potential for good electrochemical performance (Fig. S3). In order to verify our conjecture, the MoS_2/ACF cloth was sliced into round pellets with a diameter of 12 mm and used directly as free-standing electrodes in coin cells. Firstly, we examined the cyclic voltammograms (CV) behavior of the MoS_2/ACF cloth electrodes. Fig. 6a shows the initial five CV curves obtained at a scan rate of 0.2 mV s^{-1} in the voltage range of 0–3 V vs. Li^+/Li. It can be seen that there is a big difference between the first cycle and the subsequent cycles. In the first cycle, a board peak is centered at 0.95 V in the first cathodic scan, corresponding to the phase transition from trigonal prismatic (coordination of Mo by six S ions) to octahedral. Such phase transition is due to the insertion of Li ions into the MoS_2 layers, resulting in the formation of $LiMoS_2$. This peak disappears from the second cathodic sweep because only nearly amorphous MoS_2 is reformed after the charging process (lithium extraction) in the first cycle.[31, 32] A board shoulder begins to evolve from 0.72 V, which can be attributed to the insertion of additional Li^+ ions within the expanded MoS_2 structure or in the defect sites of MoS_2.[33, 34] The other peak centered around 0.1 V or lower is considered to originate from two aspects: one is the deposition of Mo metal along with the formation of Li_2S is based on the conversion reaction $MoS_2 + 4Li + 4\ e^- \rightarrow Mo + 2Li_2S$, while the other is the formation of a gel-like polymer layer resulting from electrochemically driven electrolyte degradation.[35, 36] The slight shifts in the reduction peak potentials or changes in the reduction peak shape could be caused by the overlap of the electrochemical lithium storage in both MoS_2 and ACF cloth. This peak changed to 0.21 V during subsequent cycling. In the anodic scan, the oxidation at 1.76 V can be attributed to the oxidation of Mo to MoS_2, and the following peak located at 2.42 V is associated with the oxidation of Li_2S to S. Therefore, after the first cycle, the electrode can be regarded as a mixture of S and Mo instead of the original MoS_2.[31, 33, 37, 38]

In the subsequent cathodic sweeps, the redox potentials are quite different from those observed in the first cycle. Three new reduction peaks centered at 2.12, 1.88 and 1.09 V appear, indicating

a multistep lithium insertion mechanism. The peaks centered at 2.12 and 1.88 V can be ascribed to the conversion of elemental sulfur to polysulfides and then to Li_2S, respectively. The peak at 1.09 V is attributed to the association of Li with Mo. The CV curves of the second and third cycles are nearly overlapped, indicating an excellent reversibility of the MoS_2/ACF cloth electrode.[33, 38, 39]

Fig. 6b displays the charge-discharge profiles of the MoS_2/ACF cloth for the first and second cycles at a current density of 200 mA g^{-1} with a cutoff voltage window of 0.005–3 V. It can be seen that there are two plateaus located at around 1.2 and 0.7 V, suggesting the two lithiation processes of MoS_2. The other two plateaus observed at around 1.7 and 2.2 V during charge process correspond to the reversible Li^+ extraction, agreeing well with the CV curves. The inconspicuous potential plateau obtained during the second discharge of the MoS_2/ACF cloth may be caused by low crystallinity; however, a plateau at 2.2 V during the second charge can be clearly identified.[33, 38]

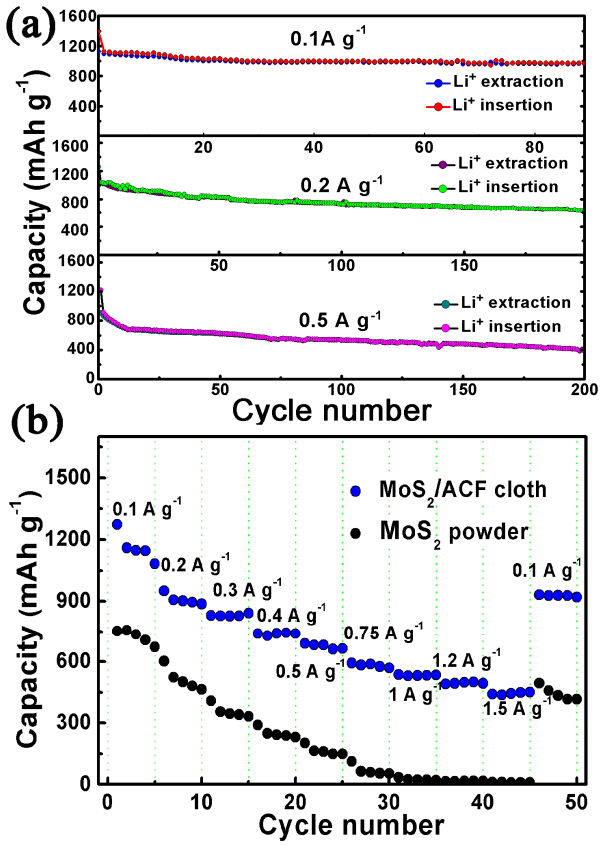

Fig. 7 (a) Cycling performance of MoS_2/ACF cloth at current densities of 0.1 A g^{-1}, 0.2 A g^{-1} and 0.5 A g^{-1}. (b) Rate performance of the MoS_2/ACF cloth under various current densities ranging from 0.1 to 1.5 A g^{-1}.

The MoS_2/ACF cloth shows good potential as an electrode material. We further examined its cycling performance and rate capability. Fig. 7a shows the specific discharge capacities over cycling at current densities of 0.1, 0.2 and 0.5 A g^{-1}. The capacities in the first cycle are 1392, 1262 and 1222 mAh g^{-1} at 0.1, 0.2 and 0.5 A g^{-1}, respectively. The corresponding charge capacities are 1125, 1036 and 908 mAh g^{-1}, respectively, which is much better than the commercial MoS_2 powders (Fig. S5). It is clear that the irreversible capacity loss during the first cycle is about 267 mAh g^{-1}, which is mainly due to the formation of the solid electrolyte interphase (SEI) layer and incorporation of Li in the defect sites of MoS_2. However, in the subsequent cycles, the Columbic efficiency reaches nearly 100%. Besides the higher specific capacity in the initial cycle, the MoS_2/ACF cloth shows good cycling performance. After 90 cycles under 0.1 A g^{-1}, the discharge capacity still remains at 971 mAh g^{-1}, indicating a capacity retention of 86.3% when compared to the second cycle, and the capacity fading rate is 0.15% per cycle. The MoS_2/ACF cloth also displays a good stability when cycled at 0.2 A g^{-1}. After 200 cycles, the discharge capacity is maintained at 635 mAh g^{-1}. Even at a high current density of 0.5 A g^{-1}, the capacity reaches 418 mAh g^{-1} after 200 cycles. The MoS_2/ACF cloth shows a superior cycling performance as compared to the reported MoS_2/carbon composites,[15, 16, 32, 36, 40-43] and even to the similar MoS_2/carbon fiber composite fabricated by a hydrothermal process.[22]

Fig. 7b shows the rate capability at various current densities from 0.1 to 1.5 A g^{-1} for the MoS_2/ACF cloth. The specific capacities are 1173, 951, 831, 739, 689, 593, 537, 491 and 441 mAh g^{-1} at 0.1, 0.2, 0.3, 0.4, 0.5, 0.75, 1, 1.2 and 1.5 A g^{-1}, respectively. Even after several cycles at various current densities, the MoS_2/ACF cloth electrode retains a capacity of 450 mAh g^{-1}. Compared to the commercial MoS_2 powder, the hieratical MoS_2/ACF cloth electrode shows a much higher capacity. Usually, the capacity of the commercial MoS_2 is less than 50 mAh g^{-1} if the current density is higher than 1 A g^{-1}. Moreover, the superior performance of MoS_2/ACF cloth electrode is also evidenced by the easy capacity recovery after cycling. The capacity is recovered up to 930 mAh g^{-1} if the current density is returned back to 0.1 A g^{-1} after cycling at various current densities ranging from 0.1 to 1.5 A g^{-1}.

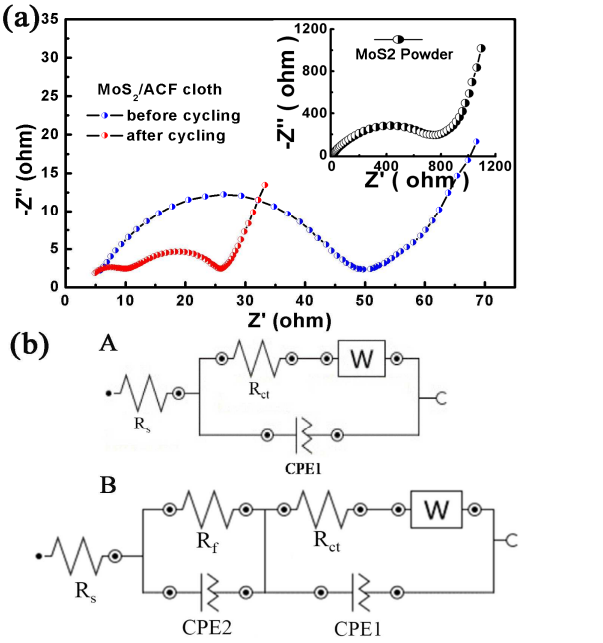

Fig. 8 (a) Nyquist plots of the MoS_2/ ACF cloth electrode before and after cycling and that of the MoS_2 powder electrode obtained by applying a sine wave with an amplitude of 5.0 mV within a frequency range from 100 KHz to 0.1 Hz at open circuit voltage. (b) Equivalent circuit model corresponding to the Nyquist plots of the MoS_2/ ACF cloth electrode (A) before and (B) after cycling.

Electrochemical impedance spectroscopy (EIS) was performed to reveal why the hierarchical MoS_2/ACF cloth shows excellent electrochemical performance. The Nyquist plots of the MoS_2/ACF electrode before and after 200 cycles at 0.5 A g^{-1} is shown in Fig. 8a. It is clear that the MoS_2/ACF cloth electrode exhibits a much lower charge transfer resistance than the MoS_2 powder, which can be attributed to the enhanced conductivity of the MoS_2/ACF cloth. Moreover, the charge transfer resistance reduces by half after 200 cycles.

The equivalent circuit model was used to fit the Nyquist plots, as shown in Fig. 8b. The intercept on Z_{real} axis in the high-frequency region corresponds to the resistance of electrolyte (R_s). The semicircle in the high-frequency region before cycling reflects the charge transfer resistance (R_{ct}) and the constant phase element (CPE1), which is related to the electrode/electrolyte interface. The oblique inclined line in the low-frequency region represents the Warburg impedance (Z_w), which is related to the solid-state diffusion of Li ions in the electrode materials. In the Nyquist plots obtained after running for 200 cycles, a new semicircle appears in the high-frequency range because of the formation of the SEI film. The resistance of the SEI film (R_f) and the constant phase element (CPE2) are associated with the resistance and CPE1 of the SEI film.[16, 17, 37]

The fitted impedance parameters are listed in Table 1. The MoS_2 powder electrode shows an R_{ct} of 855 Ω, much larger than that of MoS_2/ACF. For the MoS_2/ACF electrode, the R_s value is 4.9 Ω before cycling, and drops to 3.3 Ω after cycling; the R_{ct} before cycling is 41.7 Ω, but drops to a much lower value of 17.6 Ω after cycling. After cycling, the value of R_f of MoS_2/ACF is only 6.9 Ω. This confirms that the incorporation of the ACF cloth can greatly enhance the conductivity of MoS_2 and hence expedite the electron transport during the electrochemical lithium insertion/extraction reaction, leading to significant improved electrochemical performances. On the other hand, the MoS_2/ACF cloth is quite stable over cycling. The morphology is almost unchangeable after running at 0.5 A g^{-1} for 200 cycles (see Fig. S6). From Fig. S6c, we can see that a uniform SEI film is covered on the ACF surface, which is consistent with the EIS analysis.

electrode	R_s(Ω)	R_{ct}(Ω)	CPE1(uF)	R_f(Ω)	CPE2(uF)
MoS_2 particle before cycling	4.26	855	29.7		
MoS_2/ACF cloth before cycling	4.95	41.72	22.71		
MoS_2/ACF cloth after cycling	3.27	16.7	1.04	6.89	23.8

Table 1 Impedance parameters derived using the equivalent circuit model for MoS_2 particle and MoS_2/ACF cloth electrode before and after cycling

The stability of the MoS_2/ACF cloth is responsible for the good cycling performance. The soft and flexible ACF cloth can buffer the volume expansion of MoS_2, while the interconnected carbon fibers can serve as channels for electron transport. The direct use of the MoS_2/ACF cloth as an anode means that there is no need to use the slurry and current collector, i.e., the anode is binder-free and free-standing, which makes it easy and simple to fabricate the cells. Moreover, the ultrathin MoS_2 nanosheets guarantees the fast Li-ion diffusion, while the porous surface of ACF cloth enables electrolyte penetration and further facilitates the Li-ion transport. Therefore, such novel MoS_2/ACF cloth shows high reversible capacity, excellent cyclic stability and rate capability.

Conclusion

In summary, a novel hierarchically structured MoS_2/ACF cloth was fabricated for the first time via a simple dissolution and sintering process, and directly used as binder-free and free-standing anode for LIBs. Ultrathin MoS_2 nanosheets were uniformly grown on the surface of carbon fibers. The flexible ACF cloth acts as both a conductive template and a stabilizer. Our experiments show that the MoS_2/ACF anode exhibits high specific capacity and good electrochemical reversibility. The discharge capacity at 0.1 A g^{-1} is maintained at 971 mAh g^{-1} with a fading rate of 0.15% per cycle within 90 cycles. The interconnected carbon fibers can provide a conductive pathway for electron transport, while the ultrathin MoS_2 and the porous surface of cloth can facilitate Li-ion diffusion. Moreover, the flexibility of the cloth can restrain the volume expansion of MoS_2 caused by lithium intercalation. It is the synergistic effect between MoS_2 and ACF cloth that leads to superior electrochemical performance. We believe that the hierarchically nanostructured MoS_2/ACF cloth is a promising anode material for high-performance LIBs. The preparation method developed in this work is also applicable for other functional materials used in supercapacitors, catalysts, etc.

Acknowledgment

The authors gratefully acknowledge the financial support by the National High-Tech Research and Development Program of China (863 program) (Grant No. 2013AA119102), the Natural Science Foundation of China (Grant No. 21175050). Qinghai province science and technology support program (2012-G-Y28). They are also grateful to Anhui Jia Li Qi Aerospace Carbon fiber Co, Ltd. for the free supporting of active carbon fiber cloth.

Notes and references

[a] *College of Chemistry and Molecular Engineering, Peking University, Beijing, P. R. China. Fax: 86-10-62754680; Tel: 86-10-62754680; E-mail: chenjitao@pku.edu.cn; zhouhh@pku.edu.cn.*

[b] *Key Laboratory for Advanced Battery Materials and System (MOE), School of Materials Science and Engineering, Huazhong University of Science and Technology (HUST), Wuhan, Hubei 430074, China. Fax: 86-27-87558241; Tel: 86-27-87558241; Email: huangyh@mail.hust.edu.cn*

† Electronic Supplementary Information (ESI) available: Experimental details of making MoS_2 powder into electrode. Fig. S1–S6: XPS survey, SEM, scheme of electron and lithium ion transport in MoS_2/ACF cloth and electrochemical data of MoS_2 powder. See DOI: 10.1039/b000000x/.

‡ Footnotes should appear here. These might include comments relevant to but not central to the matter under discussion, limited experimental and spectral data, and crystallographic data.

1. M. Armand and J. M. Tarascon, *Nature*, 2008, 451, 652-657.
2. J. M. Tarascon and M. Armand, *Nature*, 2001, 414, 359-367.
3. V. Etacheri, R. Marom, R. Elazari, G. Salitra and D. Aurbach, *Energy Environ. Sci.*, 2011, 4, 3243-3262.
4. E. Benavente, M. A. Santa Ana, F. Mendizábal and G. González, *Coord. Chem. Rev.*, 2002, 224, 87-109.
5. J. Feng, X. Sun, C. Wu, L. Peng, C. Lin, S. Hu, J. Yang and Y. Xie, *J. Am. Chem. Soc.*, 2011, 133, 17832-17838.
6. N. Zheng, X. Bu and P. Feng, *Nature*, 2003, 426, 428-432.

7. Z. Zeng, C. Tan, X. Huang, S. Mao and H. Zhang, *Energy Environ. Sci.*, 2014, 7, 797-804.
8. Y. Jing, Z. Zhou, C. R. Cabrera and Z. Chen, *J. Phy. Chem. C*, 2013, 117, 25409-25413.
9. X. Fang, C. Hua, C. Wu, X. Wang, L. Shen, Q. Kong, J. Wang, Y. Hu, Z. Wang and L. Chen, *Chem. Eur. J.*, 2013, 19, 5694-5700.
10. R. Dominko, D. Arčon, A. Mrzel, A. Zorko, P. Cevc, P. Venturini, M. Gaberscek, M. Remskar and D. Mihailovic, *Adv. Mater.*, 2002, 14, 1531-1534.
11. T. Stephenson, Z. Li, B. Olsen and D. Mitlin, *Energy Environ. Sci.*, 2014, 7, 209-231.
12. J. Chen, N. Kuriyama, H. Yuan, H. T. Takeshita and T. Sakai, *J. Am. Chem. Soc.*, 2001, 123, 11813-11814.
13. M. Chhowalla and G. A. Amaratunga, *Nature*, 2000, 407, 164-167.
14. C. Zhang, Z. Wang, Z. Guo and X. W. Lou, *ACS Appl. Mater. Interfaces*, 2012, 4, 3765-3768.
15. S. Ding, J. S. Chen and X. W. Lou, *Chem. Eur. J.*, 2011, 17, 13142-13145.
16. J. Z. Wang, L. Lu, M. Lotya, J. N. Coleman, S. L. Chou, H. K. Liu, A. I. Minett and J. Chen, *Adv. Energy Mater.*, 2013, 3, 798-805.
17. K. Chang and W. Chen, *ACS Nano*, 2011, 5, 4720-4728.
18. H. Yu, C. Ma, B. Ge, Y. Chen, Z. Xu, C. Zhu, C. Li, Q. Ouyang, P. Gao, J. Li, et al., *Chem. Eur. J.*, 2013, 19, 5818-5823.
19. M. Suzuki, *Carbon*, 1994, 32, 577-586.
20. B. Xu, F. Wu, S. Chen, C. Zhang, G. Cao and Y. Yang, *Electrochim. Acta*, 2007, 52, 4595-4598.
21. Y. Sun, X. Hu, J. C. Yu, Q. Li, W. Luo, L. Yuan, W. Zhang and Y. Huang, *Energy Environ. Sci.*, 2011, 4, 2870-2877.
22. H. Yu, C. Zhu, K. Zhang, Y. Chen, C. Li, P. Gao, P. Yang and Q. Ouyang, *J. Mater. Chem.A*, 2014, DOI: 10.1039/C3TA14744D.
23. K. Liu, W. Zhang, Y. Lee, Y. Lin, M. Chang, C. Su, C. Chang, H. Li, Y. Shi, H. Zhang, et al., *Nano Lett.*, 2012, 12, 1538-1544.
24. J. N. Coleman, M. Lotya, A. O'Neill, S. D. Bergin, P. J. King, U. Khan, K. Young, A. Gaucher, S. De, R. J. Smith, et al., *Science*, 2011, 331, 568-571.
25. U. K. Sen and S. Mitra, *ACS Appl. Mater. Interfaces*, 2013, 5, 1240-1247.
26. H. S. Lee, S. W. Min, Y. G. Chang, M. K. Park, T. Nam, H. Kim, J. H. Kim, S. Ryu and S. Im, *Nano Lett.*, 2012, 12, 3695-3700.
27. Y. H. Lee, X. Q. Zhang, W. Zhang, M. T. Chang, C. T. Lin, K. D. Chang, Y. C. Yu, J. T. W. Wang, C. S. Chang, L. J. Li, et al., *Adv. Mater.*, 2012, 24, 2320-2325.
28. S. K. Park, S. H. Yu, S. Woo, B. Quan, D. C. Lee, M. K. Kim, Y. E. Sung and Y. Piao, *Dalton Trans.*, 2013, 42, 2399-2405.
29. H. W. Wang, P. Skeldon and G. E. Thompson, *Surf. Coat. Technol.*, 1997, 91, 200-207.
30. J. Kibsgaard, Z. Chen, B. N. Reinecke and T. F. Jaramillo, *Nature Materials*, 2012, 11, 963-969.
31. H. Liu, D. Su, R. Zhou, B. Sun, G. Wang and S. Z. Qiao, *Adv. Energy Mater.*, 2012, 2, 970-975.
32. K. Bindumadhavan, S. K. Srivastava and S. Mahanty, *Chem. Commun.*, 2013, 49, 1823-1825.
33. J. Xiao, X. Wang, X. Q. Yang, S. Xun, G. Liu, P. K. Koech, J. Liu and J. P. Lemmon, *Adv. Funct. Mater.*, 2011, 21, 2840-2846.
34. S. K. Park, S. H. Yu, S. Woo, J. Ha, J. Shin, Y. E. Sung and Y. Piao, *CrystEngComm*, 2012, 14, 8323-8325.
35. K. Chang and W. Chen, *Chem. Commun.*, 2011, 47, 4252-4254.
36. G. Du, Z. Guo, S. Wang, R. Zeng, Z. Chen and H. Liu, *Chem. Commun.*, 2010, 46, 1106-1108.
37. K. Chang and W. Chen, *J. Mater. Chem.*, 2011, 21, 17175-17184.
38. Z. Wang, T. Chen, W. Chen, K. Chang, L. Ma, G. Huang, D. Chen and J. Y. Lee, *J. Mater. Chem.A*, 2013, 1, 2202-2210.
39. H. Hwang, H. Kim and J. Cho, *Nano Lett.*, 2011, 11, 4826-4830.
40. L. Yang, S. Wang, J. Mao, J. Deng, Q. Gao, Y. Tang and O. G. Schmidt, *Adv. Mater.*, 2013, 25, 1180-1184.
41. S. Liang, J. Zhou, J. Liu, A. Pan, Y. Tang, T. Chen and G. Fang, *CrystEngComm*, 2013, 15, 4998-5002.
42. C. Zhang, H. B. Wu, Z. Guo and X. W. Lou, *Electrochem. Commun.*, 2012, 20, 7-10.
43. S. Ding, D. Zhang, J. S. Chen and X. W. Lou, *Nanoscale*, 2012, 4, 95-98.